RSC Advances

PAPER

View Article Online
View Journal | View Issue

Cite this: *RSC Adv.*, 2018, **8**, 15991

TiO_2 surfaces self-doped with Ag nanoparticles exhibit efficient CO_2 photoreduction under visible light†

Yanzhao Zhang, Xiya Wang, Peimei Dong, Zhengfeng Huang, Xiaoxiao Nie and Xiwen Zhang *

Received 18th March 2018
Accepted 25th April 2018

DOI: 10.1039/c8ra02362j

rsc.li/rsc-advances

Doping with intrinsic defects to enhance the photocatalytic performance of TiO_2 has recently attracted attention from many researchers. In this report, we developed an original approach to realise stabilized surface doping using intrinsic defects with the loading of Ag nanoparticles (AgNPs) on the surface. Herein, atmospheric pressure dielectric barrier discharge (DBD) cold plasma was used to help load the AgNPs, and ethanol treatment was used to introduce intrinsic defects (oxygen vacancies and Ti^{3+}) on the surface of materials. This method avoids environmentally hazardous reducing regents and is undertaken under atmospheric pressure, thus reducing energy-consuming and complex operation. We combine the advantages of noble metal nanoparticles and surface doping to enhance the photocatalytic performance under the visible light. The characterization of the materials indicates that the loading of AgNPs and introduction of intrinsic defects can change the electronic structure of the composite material and improve its efficiency. The samples show significant enhancement in CO_2 photoreduction to obtain CO and CH_4, with yields reaching 141 μmol m^{-2} and 11.7 μmol m^{-2}, respectively. The formation mechanism of the method for TiO_2 modification and CO_2 reduction is also discussed.

1. Introduction

The development of TiO_2 in the CO_2 photoreduction field is restricted by the wide band gap and the high recombination rates of the electrons and holes.[1–5] Researchers have modified TiO_2 to improve its photocatalytic efficiency, mainly by three methods including making semiconductor heterojunctions,[6–8] doping[9,10] and the loading of noble metals.[11–13] Combining TiO_2 with other specific semiconductors could change the electronic structures of the composite materials and therefore restrain the recombination of the photoelectrons and holes.[14,15] In this way, these composite materials exhibit high photoreduction efficiency. However, it is always a complex process to prepare these composite materials, which has an adverse effect on this method. Loading noble metals could also be a useful approach to increase the photoreduction efficiency of TiO_2, as noted above. These noble metals, such as Ag, Au, Pt and Pd, can act as an electron trap, resulting in the separation of the photoelectrons and holes. Some of these noble metal nanoparticles can also increase the absorption of the visible-light due to their localized surface plasmon resonance effect (LSPR).[16–18]

Doping is also an efficient way to change the electronic structure of a photocatalyst to enhance its photocatalytic activity under visible light. A large amount of different elements have been doped in TiO_2 by various ways, including non-metal elements and transition metal elements. However, these doping atoms are always recombination centres during the migration of photogenerated charge carriers from the bulk to the surface.[10,19] Therefore, developing a surface doping method is also a promising approach to modifying TiO_2, and some researchers have accordingly focused on surface doping. For example, Wang *et al.* employed an etching and doping method to realise tungsten-doping on the surface of TiO_2 nanorods, which promoted its photoelectrochemical performance.[9] Chang *et al.* verified that the surface vanadium-doped TiO_2 performed efficiently than the bulk doped TiO_2.[20] Cho *et al.* applied thermal treatment to TiO_2 to realize tungsten and carbon co-doping on the surface, which improved the photoelectrochemical water splitting efficiency.[21]

Among the different elements of surface doping, self-doping (intrinsic defects: Ti^{3+} and oxygen vacancies) has attracted attention because this approach does not need to introduce foreign elements, thus avoiding contamination and pollution by chemicals. In addition, these defects always serve as the active sites during the photocatalytic process. The target substances which participate in the photoreduction or photo-oxidation can easily adsorb on these active sites, which can promote the photocatalytic process.[1,22] However, the surface

State Key Laboratory of Silicon Materials Science, School of Material Science & Engineering, Zhejiang University, Hangzhou, Zhejiang 310027, P. R. China. E-mail: zhangxw@zju.edu.cn

† Electronic supplementary information (ESI) available. See DOI: 10.1039/c8ra02362j

intrinsic defects in TiO_2 can be easily oxidized by oxygen when the photocatalyst is exposed to the air. It is common circumstance that after the photocatalyst is treated with hydrogenation methods and other methods, the surface of the material is oxidized immediately.[5,22] The oxidized surface prevents the bulk of the TiO_2 from being oxidized by the oxygen in air. Under these circumstances, the intrinsic defects are more widely present in the bulk of the material rather than on the surface. These materials can respond to the visible light due to the intrinsic defects in the bulk but they cannot help CO_2 and other target substances adsorb on the surface because of the lack of surface doping.

In order to address the problems outlined above, we herein have developed a different kind of material which can achieve steady surface self-doping. This original approach does not need to use high pressure and toxic chemicals, thus avoiding high energy consumption, toxicity and pollution. This method is based on ethanol treatment and a DBD cold plasma technique. The ethanol treatment process can introduce the intrinsic defects into the TiO_2 and the DBD cold plasma with AgNPs loading can help stabilize the surface doping.

2. Experimental section

2.1. Materials

Commercial Ti-foil which was of 99.9% purity was purchased from XinXin Metal Material Company, China. Silver nitrate ($AgNO_3$), hydrochloric acid (HCl, 36%), ethanol (C_2H_6O) and ammonium hydroxide ($NH_3 \cdot H_2O$, 26%) were purchased from China Experiment Reagent Co., Ltd. (analytical grade) and were used without further purification.

2.2. Deposition of Ag nanoparticles on TiO_2 film

The TiO_2 film was prepared through the method which was recently reported by our group using pristine TiO_2 in the experiments.[23] The deposition of the Ag nanoparticles was accomplished by a simple two-step method that is illustrated in Scheme 1. The as-prepared TiO_2 film was immersed into the $AgNO_3$ solution of a certain concentration (50 mL). Then, 0.15 M $NH_3 \cdot H_2O$ was added dropwise into the solution under magnetic stirring (Scheme 1(a)). The film was kept in the solution for 15 min until its colour changed to brown and then dried in air.

Subsequently the sample was reduced by the DBD cold plasma method. Scheme 1(b) shows the diagram of the DBD cold plasma device. The voltage can be applied to the reactor by two electrodes which are put on the two sides of the quartz glass of the reactor. A mixture of hydrogen and argon (weight ratio 1 : 1) was pumped into the reactor (50 mL min^{-1}). The power source supplied a bipolar sine wave output of 45–200 W at a frequency of 10–20 kHz. The DBD plasma treatment lasted for 30 s. The weight of silver nitrate was controlled to be variously 0.01 g, 0.02 g and 0.03 g, and the corresponding resulting samples were labelled as AP1, AP2 and AP3, respectively.

Additionally, three samples loaded with the same amount of Ag_2O as AP1, AP2 and AP3 were treated by heated ethanol before they were reduced by the DBD cold plasma. Each sample was put into a porcelain boat with 10 mL ethanol and covered by another porcelain boat. They were then calcined in a muffle furnace at the heating rate of 10 °C min^{-1}. The samples were kept at 200 °C for 60 min and then naturally cooled. Finally they were treated by DBD cold plasma as mentioned above. The corresponding resulting samples were labelled as ACP1, ACP2 and ACP3, respectively.

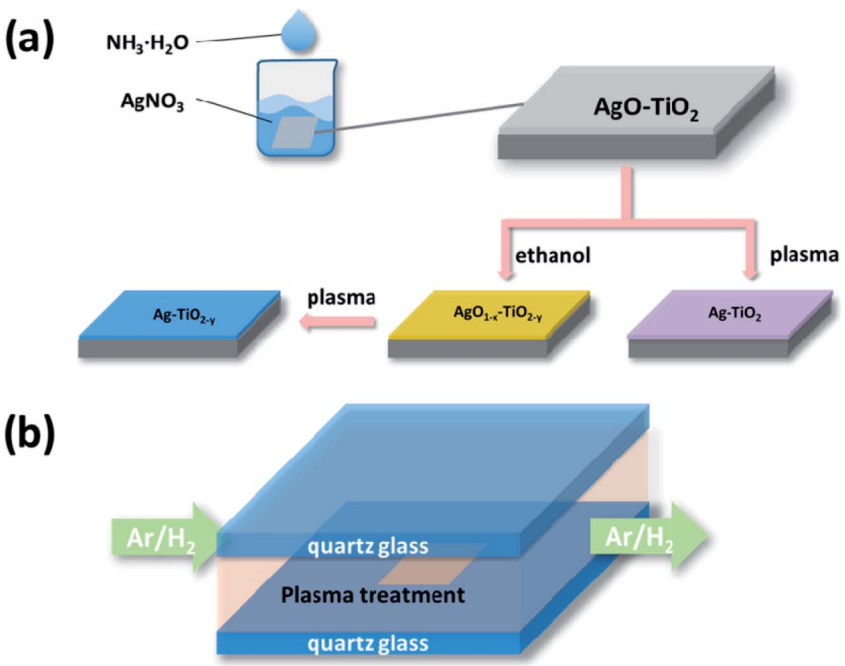

Scheme 1 Schematic illustration of the deposition processes of AgNPs (a) and the subsequent DBD cold plasma treatment undertaken at atmospheric pressure (b).

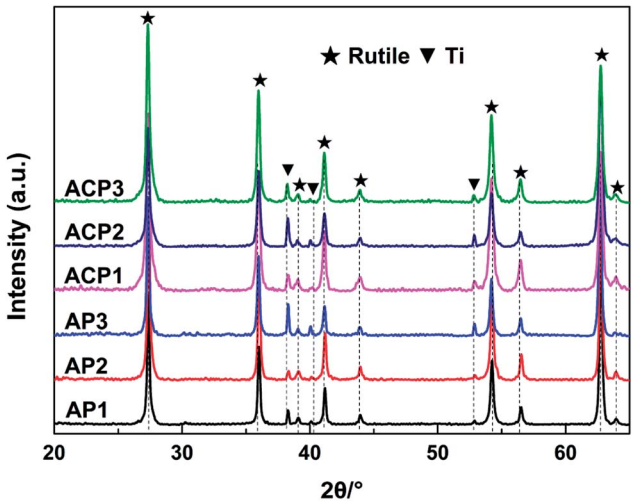

Fig. 1 XRD patterns of the different samples. ▼: Ti metal and ★: rutile phase of TiO_2.

2.3. Characterisation

The morphologies of the fabricated samples were examined using scanning electron microscopy (SEM, Hitachi S4800) and transmission electron microscopy (TEM, JEM 2100F). The dispersion of elements (Ag, Ti, and O) on the Ag/TiO_2 samples was analyzed by an energy dispersive spectrometer (EDS). The crystal phases of all as-prepared samples were determined using X-ray diffraction (XRD), which was performed on an X′ Pert PRO X-ray diffractometer equipped with Cu Kα radiation ($\lambda = 0.1541$ nm). X-ray photoelectron spectroscopy (XPS) was performed on a VG ESCALAB Mark II instrument using Mg-Kα (photon energy = 1253.6 eV) as the excitation source, and its energy analyser working at 50 eV with the overall resolution of 0.2 eV. Due to relative surface charging, the binding energy displayed a shift which was rectified using the C 1s binding energy of 284.6 eV as an internal standard. UV-vis diffuse reflectance spectra of the samples were obtained using a UV-vis spectrophotometer (Shimadzu UV-3600, Japan). $BaSO_4$ was used as a reflectance standard in the UV-vis diffuse reflectance experiments. Raman spectra were obtained on a LabRam HRUVat room temperature.

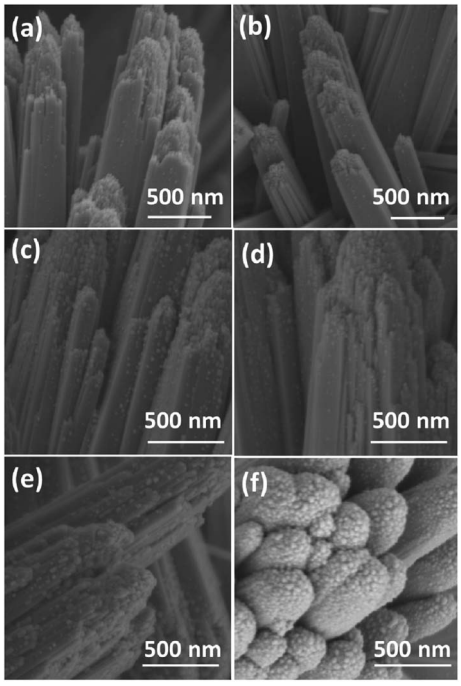

Fig. 2 SEM images of the samples: AP1 (a); AP2 (c); AP3 (e); ACP1 (b); ACP2 (d); ACP3 (f).

2.4. Photoreduction testing

The CO_2 photoreduction experiments with H_2O vapor were carried out in a self-assembled reactor (capacity 4500 mL) as reported in our previous study.[23] The as-prepared samples were placed at the centre of the reactor under the illumination of two 300 Watt xenon lamp simulated solar light sources. A 350 W ultraviolet lamp was used as the ultraviolet source with the wavelength shorter than 420 nm. Before illumination, ultra-pure CO_2 (Air Products, 99.995%) was pumped into the reactor at a flow rate of 300 mL min^{-1} for 1 h to purge residual air with a flask filled with de-ionized water to add the H_2O vapour into the reactor. After purging, illumination commenced and the CO_2 flow was stopped. The gaseous products in the reactor were periodically analyzed by gas chromatography (GC/FID, Thermo-Fisher, Trace GC). The room temperature remained at 25 °C during the testing.

3. Results and discussion

The surface self-doping process on the TiO_2 film occurs mainly by three steps. In the first step, Ag_2O nanoparticles are deposited on the surface of the film by a chemical precipitation method. The $AgNO_3$ solution reacts with ammonium hydroxide to generate Ag_2O nanoparticles and these nanoparticles are deposited on the surface of the film. In the ethanol treatment process, the TiO_2 and Ag_2O will be partly reduced by the ethanol (Fig. S1; see ESI†). In this process, ethanol liquid becomes gas under 200 °C and the hydroxyl group of the ethanol gas reacts with an oxygen atom in TiO_2 to produce acetaldehyde and water, leaving an oxygen vacancy in the crystal lattice, which was revealed in a previous report.[10] The main function of the DBD cold plasma is to totally reduce the Ag_2O nanoparticles. After this process, the Ag_2O nanoparticles are totally reduced to AgNPs and the intrinsic defects in the TiO_2 film are preserved.

The crystal structures of the six samples were investigated by their corresponding XRD patterns. All of the sample types exhibited a rutile phase (JCPDS card no. 21-1276, Fig. 1). The diffraction peaks appearing at $2\theta = 27.4°$, 36.1°, 39.1°, 41.2°, 44.1°, 54.3°, 56.6°, 62.74° and 64.03° are attributed to the (110), (101), (200), (111), (210), (211), (220), (002) and (310) lattice planes of the rutile phase, respectively. In addition, the diffraction peaks at $2\theta = 38.4°$, 40.2° and 53.0° are attributed to the (002), (101), and (102) lattice planes of the Ti metal (JCPDS card no.44-1294), respectively. The sharp diffraction peaks of

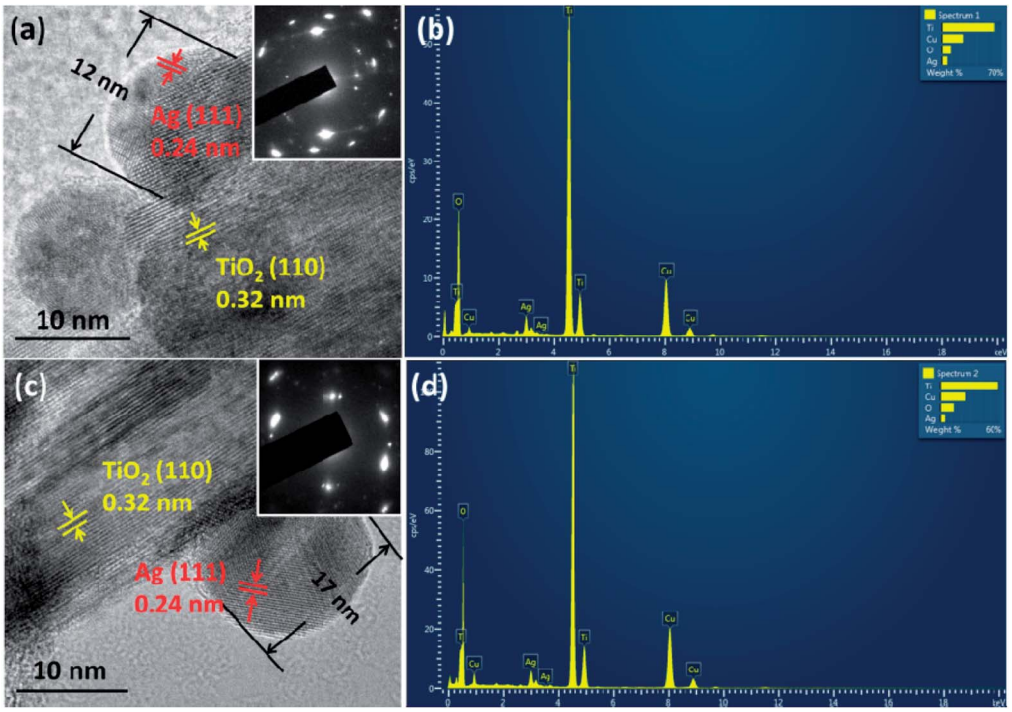

Fig. 3 HRTEM images of the samples: AP2 (a) and ACP2 (c). The insets are their corresponding SAED patterns; (b) (d): EDS spectra of AP2 and ACP2, respectively.

the XRD patterns reveal that the TiO_2 films have good crystallinity. There are no peaks attributed to silver detected in any of the samples. The reason for this may be that the levels of the deposited AgNPs of small diameter are too low to be detected by XRD. This may also illustrate the uniform distribution of the AgNPs. The perfect match of the XRD patterns suggests that neither the process of the DBD plasma nor the annealing in ethanol significantly affected the crystalline structures of the TiO_2 film (Fig. 1).

The morphologies of the films were observed by SEM (Fig. 2 and S2†). The film consists of rutile nanorods with loaded AgNPs. These sliver nanoparticles are distributed homogeneously on the surface of the TiO_2 nanorods and the diameter of the nanoparticles is typically smaller than 20 nm. With increasing concentration of the $AgNO_3$ solution, the density of AgNPs becomes higher. A single deposited Ag nanoparticle and TiO_2 nanorods are further revealed by TEM and HRTEM in Fig. 3. AgNPs deposited on the AP2 (Fig. 3a) were not calcined and the lattice fringes of 0.24 nm can be attributed to the (111) plane of metallic silver. The TiO_2 nanorods can be revealed by the 0.32 nm spacing which is attributed to the rutile phase in the (110) plane. According to the SAED pattern of AP2, the rutile phase is a kind of perfect single crystal whose crystal defects are less than those of the polycrystalline phase. This is

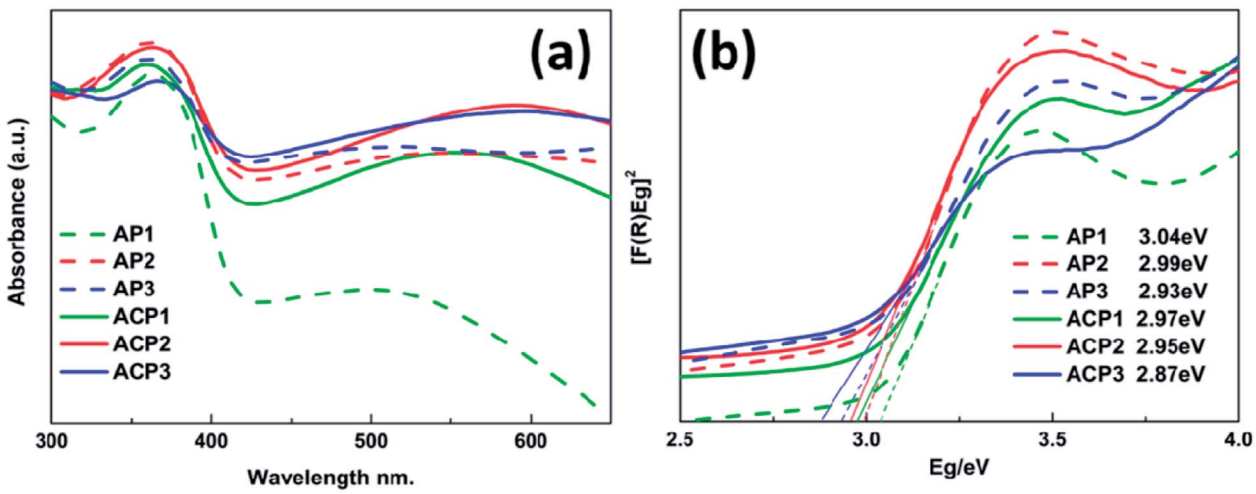

Fig. 4 UV-vis diffuse reflectance spectra (a) and Tauc plots with their band gap values (b).

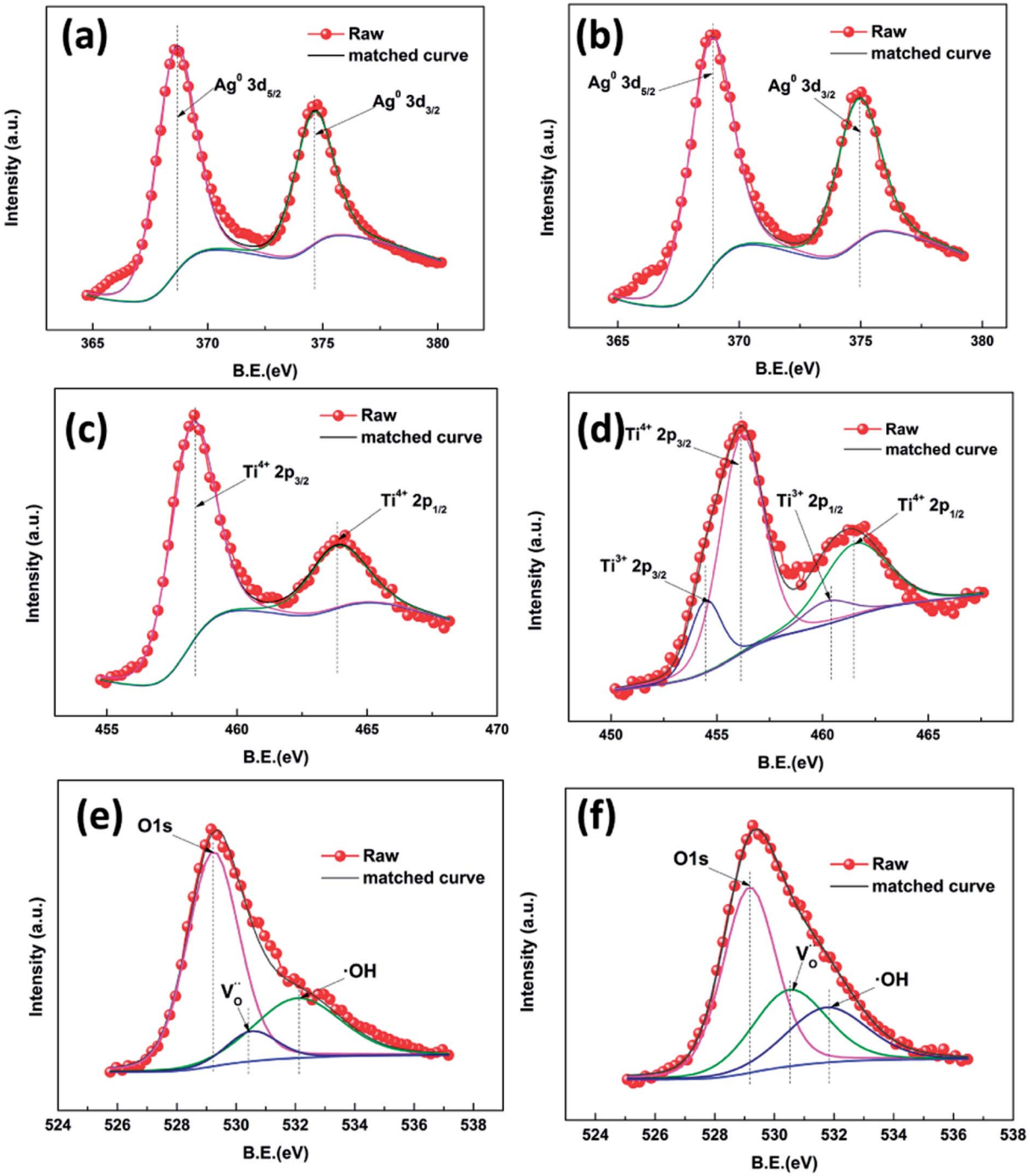

Fig. 5 High resolution XPS spectra of Ag 3d of different samples: AP1 (a) and ACP1 (b);Ti 2p: AP1 (c) and ACP1 (d); O 1s: AP1 (e) and ACP1 (f).

an important characteristic that can reduce the recombination of the photoelectrons and holes, which helps improve the photocatalytic efficiency. The EDS spectrum of AP2 (Fig. 3b) reveals its elemental composition. The elemental copper originates from the TEM sample holding grid and Ti, O, and Ag are from the sample AP2. The spectrum also illustrates that the present experimental approach can help avoid contamination by impurity elements. The HRTEM image of ACP2 (Fig. 3c) and the EDS spectrum (Fig. 3d) are nearly the same as those of AP2.

Comparison between AP1–3 and ACP1–3 indicates that their SEM images are nearly the same with regard to the density of AgNPs, which also verifies that the ethanol treatment and DBD plasma did not change the morphology and microstructure of the films.

The UV-vis spectra of various samples are shown in Fig. 4a and the corresponding band gap values are also indicated by Tauc plots in Fig. 4b. These samples are characterized by strong absorption in the UV region (below 410 nm wavelength), which

is a typical rutile TiO_2 absorption.[24–26] It is apparent that the deposited AgNPs can expand the absorption of these films and with the increasing amount of the deposited AgNPs, these samples have better response to visible-light (above 420 nm wavelength). In addition, the absorption edges of these samples also have a slight red shift due to the deposited AgNPs; this trend becomes more significant with the increasing concentration of the AgNPs, which is consistent with results of the SEM images. Compared to the AP1–3 series of samples, the ACP1–3 series of samples exhibits more positive response to the visible light which may be owing to the introduction of the surface doping intrinsic defects that can be revealed by XPS and Raman spectra. There is a wide absorption range from about 460 nm to 600 nm with peaks at about 540 nm, which is attributed to the LSPR effect of the metallic sliver nanoparticles.[16–18] The UV-vis spectrum of pristine TiO_2 film is shown in the Fig. S3† which indicates that AP and ACP samples increase the visible light absorption.

As can be seen in Fig. S4,† peaks attributed to Ag, O, Ti and C are present, which is consistent with the EDS results indicating the existence of these pure elements. High resolution XPS was employed to investigate the surface chemical bonding of the samples (Fig. 5). Fig. 5a and b show Ag 3d high resolution XPS spectra of samples AP1 and ACP1, respectively. In these two spectra, there are only two symmetrical peaks at 367.9 eV and 373.9 eV which can be attributed to Ag^0 $3d_{5/2}$ and $3d_{3/2}$, respectively.[27–29] Their spin energy separation is 6.0 eV, which means that the AgNPs exist as metallic silver. These results confirm the results of the crystal plane in the HRTEM images, indicating that the DBD plasma can thoroughly reduce the Ag^+ to Ag^0. The spectra in Fig. 5c and d show Ti 2p states with binding energies of 458.22 and 463.85 eV, consistent with the standard $2p_{3/2}$ and $2p_{1/2}$ binding energies, respectively for Ti^{4+} in rutile. The XPS spectra of ACP1 are different from those of AP1. The spectrum in Fig. 5d shows not only the peak of the Ti^{4+} 2p states but also the binding energies of 457.59 and 462.83 eV which are consistent with the standard $2p_{3/2}$ and $2p_{1/2}$ binding energies for Ti^{3+}, respectively.[30–33] These results illustrate that the ethanol treatment has introduced Ti^{3+} into the films. Samples AP1 and ACP1 show an O 1s state with a binding energy of 529.49 eV, consistent with the standard binding energy for O in rutile. This peak has two shoulders at 530.79 and 531.99 eV attributed to an oxygen vacancy and surface hydroxyl band, respectively.[30–32] There were oxygen vacancies (Fig. 5e) found in sample AP1. According to the previous reports, the numerous un-coordinated O atoms existing on the surface of the rutile can facilitate the formation of oxygen vacancies. However, it is apparent that the shoulder peak attributed to oxygen vacancy (Fig. 5f) accounts for a greater proportion in sample ACP1, which illustrates that the ethanol treatment can introduce oxygen vacancies in rutile. As the detection depth of XPS is restricted to several nanometers below the surface of TiO_2, the results indicate that these intrinsic defects are distributed mainly on the surface. The additional experiment (Fig. S5†) also illustrates that the AgNPs help introduce these intrinsic defects onto the surface of the samples.

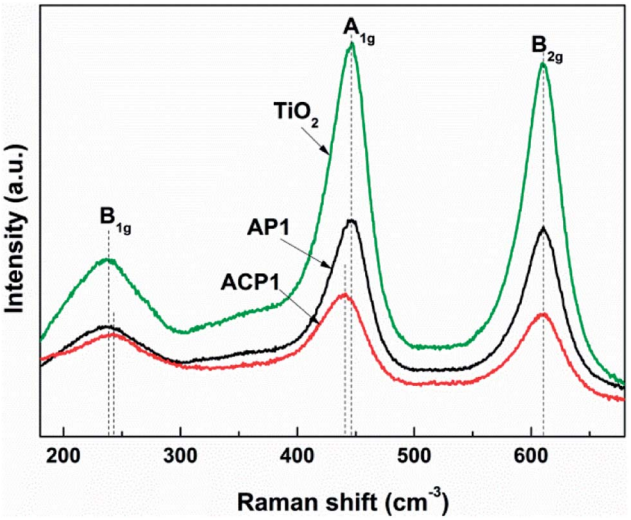

Fig. 6 Raman spectra of the different samples.

In order to obtain better confirmation on the presence of intrinsic defects, Raman spectra of the samples (Fig. 6) were also observed. Three typical Raman bands at 230 (B_{1g} mode), 440 (A_{1g} mode), and 610 (B_{2g} mode) cm^{-1} are observed which are attributed to rutile.[34,35] The results of the phase composition revealed from the Raman spectra also corroborate the XRD results. Compared with the Raman spectra of pristine TiO_2 and AP1, the Raman spectrum of ACP1 shows a clear blueshift at 230 (B_{1g} mode) and redshift at 440 cm^{-1} (A_{1g} mode). At the same time, the peak at 610 cm^{-1} (B_{2g} mode) does not show any difference among these three samples. According to a previous report, these phenomena indicate that the sample ACP1 was doped with intrinsic defects by the ethanol treatment.[35] However, the sample AP1 that has not been treated with ethanol conforms to the pristine TiO_2, which means that intrinsic defects have not been introduced into the sample AP1. These results are in good accordance with those from the XPS and UV-vis spectra.

Fig. 7 shows the CO_2 photoreduction activity of the different samples in the presence of H_2O vapor under the influence of visible light. Before the experiments, blank tests were performed, which consisted of measurements of light-illuminated CO_2 + H_2O without the photocatalyst, CO_2 + H_2O with the photocatalyst in the dark, and light-illuminated photocatalyst in H_2O without CO_2, respectively, and no target products were detected in the blank tests. It is obvious that the samples ACP1–3 exhibits higher photocatalytic efficiency than samples AP1–3 under both two kinds of light. The highest CO and CH_4 production rates of ACP3 are about 141 μmol m^{-2} and 11.7 μmol m^{-2} under simulated solar light, respectively, while the production rates of AP3 are about 88 μmol m^{-2} and 7.9 μmol m^{-2}. The highest CO and CH_4 production rates of ACP3 are about 47 μmol m^{-2} and 5.5 μmol m^{-2} under visible light, respectively, while the production rates of AP3 are about 37 μmol m^{-2} and 4.6 μmol m^{-2}. The samples that deposited Ag nanoparticles exhibit excellent photocatalytic performance

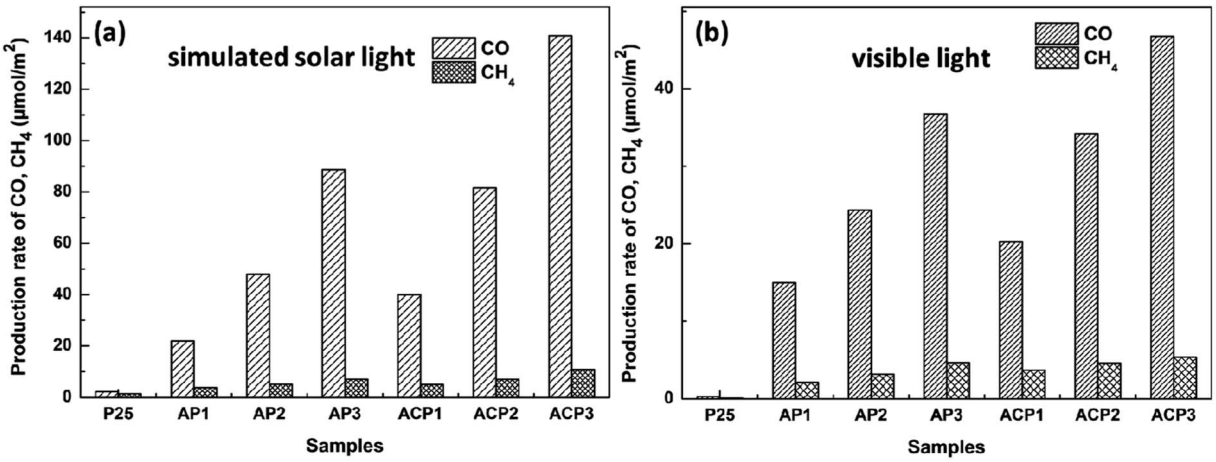

Fig. 7 Evolution of CO and CH_4 yields of different samples under simulated solar light (a) and visible light (b).

compared with the P25 under visible light, which should be attributed to the LSPR effect of the Ag nanoparticle. This is also consistent with the results of the UV-vis spectra.

The probable mechanism of the enhanced photocatalytic activity may be due to the following explanation. The AgNPs deposited on the TiO_2 surface are motivated by the visible light due to the LSPR effect. The photoelectron flow injects into the conduction band (CB) of TiO_2, causing separation between electrons and holes, attributed to the Schottky barrier between TiO_2 and AgNPs.[36–39] The resulting LSPR effect can also promote the charge migration by producing the local surface electronic field and restraining the recombination of electrons and holes.[38,40,41] TiO_2 nanorods act as electron acceptors, and the reactants H_2O and CO_2 adsorbed on the surface of the nanorods will react with the electrons.[1,22] The reason for the higher photocatalytic efficiency of sample ACP1–3 is due to the surface doping. The surface defects will act as adsorption and reaction sites. CO_2 molecules adsorbed on the surface of the TiO_2 film accept the separated electrons to produce an anion radical. The different possible products obtained are a result of the consuming of different numbers of electrons. As shown in Scheme 2, one CH_4 molecule obtained consumes more electrons (8H) than the generation of CO (2H). The CO is not only a product but also a reactant of the CH_4. As a result, the yield of CO is generally much higher than that of CH_4.[42,43]

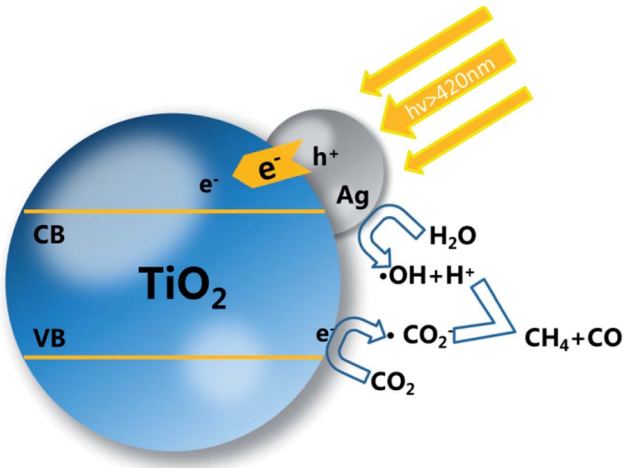

Scheme 2 Schematic of mechanism for photocatalytic process of TiO_2 decorated with AgNPs and surface self-doping.

4. Conclusions

In conclusion, Ag–TiO_2 films with surface self-doping of intrinsic defects were obtained by a facile method involving ethanol treatment as the reducing reagent to realize the self-doped films. The films with AgNPs and intrinsic defects have broadened response to visible light and promote the adsorption of reactive reagents, thus enhancing the photocatalysis performance of the films for reduction of CO_2 to CO and CH_4 under visible light. The highest yields of CO and CH_4 under visible light were about 141 μmol m^{-2} and 11.7 μmol m^{-2}, respectively. The loaded AgNPs change the band gap of the photocatalyst which broadens the absorption of the film in the visible light and the near-infrared regions, thereby achieving photocatalytic activity. The deposited AgNPs are likely to help stabilize the surface intrinsic defects, which can promote the photoreduction on the surface. These results indicate that the composite films presented herein may be a way to combine the advantages of noble metal addition and self-doping. We hold the opinion that the deposited noble metal nanoparticles can have an impact on the surface self-doping, which should be further studied. It is an edification for researchers who are interested in TiO_2 self-doping and noble metal deposition.

Conflicts of interest

The authors declare that there is no conflict of interest.

References

1 X. Pan and Y.-J. Xu, *J. Phys. Chem. C*, 2013, **117**, 17996–18005.
2 X. Chen, L. Liu, P. Y. Yu and S. S. Mao, *Science*, 2011, **331**, 746–750.

3 Z. Wang, C. Yang, T. Lin, H. Yin, P. Chen, D. Wan, F. Xu, F. Huang, J. Lin, X. Xie and M. Jiang, *Energy Environ. Sci.*, 2013, **6**, 3007–3014.
4 H. Cui, W. Zhao, C. Yang, H. Yin, T. Lin, Y. Shan, Y. Xie, H. Gu and F. Huang, *J. Mater. Chem.*, 2014, **2**, 8612–8616.
5 Y. Zhou, C. Chen, N. Wang, Y. Li and H. Ding, *J. Phys. Chem. C*, 2016, **120**, 6116–6124.
6 C. Y. Su, C. C. Wang, Y. C. Hsueh, V. Gurylev, C. C. Keic and T. P. Perng, *Nanoscale*, 2015, **7**, 19222–19230.
7 L. Wang, S. Liu, Z. Wang, Y. Zhou, Y. Qin and Z. L. Wang, *ACS Nano*, 2016, **10**, 2636–2643.
8 Y. J. Yuan, Z.-J. Ye, H.-W. Lu, B. Hu, Y. H. Li, D.-Q. Chen, J.-S. Zhong, Z.-T. Yu and Z.-G. Zou, *ACS Catal.*, 2016, **6**, 532–541.
9 Y. Wang, Y.-Y. Zhang, J. Tang, H. Wu, M. Xu, Z. Peng, X.-G. Gong and G. Zheng, *ACS Nano*, 2013, **7**, 9375–9383.
10 L. Kong, Z. Jiang, C. Wang, F. Wan, Y. Li, L. Wu, J.-F. Zhi, X. Zhang, S. Chen and Y. Liu, *ACS Appl. Mater. Interfaces*, 2015, **7**, 7752–7758.
11 K. Lee, R. Hahn, M. Altomare, E. Selli and P. Schmuki, *Adv. Mater.*, 2013, **25**, 6133–6137.
12 J. Fei and J. Li, *Adv. Mater.*, 2015, **27**, 314–319.
13 R. Dong, Q. Zhang, W. Gao, A. Pei and B. Ren, *ACS Nano*, 2016, **10**, 839–844.
14 T. J. Athauda, J. G. Neff, L. Sutherlin, U. Butt and R. R. Ozer, *ACS Appl. Mater. Interfaces*, 2012, **4**, 6916–6925.
15 X. Chen, J. Wei, R. Hou, Y. Liang, Z. Xie, Y. Zhu, X. Zhang and H. Wang, *Appl. Catal., B*, 2016, **188**, 342–350.
16 H. Zhang, G. Wang, D. Chen, X. J. Lv and U. H. Jinghong, *Chem. Mater.*, 2008, **20**, 6543–6549.
17 J. H. He, I. Ichinose, T. Kunitake and A. Nakao, *Langmuir*, 2002, **18**, 10005–10010.
18 K. Awazu, M. Fujimaki, C. Rockstuhl, J. Tominaga, H. Murakami, Y. Ohki, N. Yoshida and T. Watanabe, *J. Am. Chem. Soc.*, 2008, **130**, 1676–1680.
19 M. Kong, Y. Li, X. Chen, T. Tian, P. Fang, F. Zheng and X. Zhao, *J. Am. Chem. Soc.*, 2011, **133**, 16414–16417.
20 S.-m. Chang and W.-s. Liu, *Appl. Catal., B*, 2011, **101**, 333–342.
21 I. S. Cho, C. H. Lee, Y. Feng, M. Logar, P. M. Rao, L. Cai, D. R. Kim, R. Sinclair and X. Zheng, *Nat. Commun.*, 2013, **4**, 1723.
22 L. Liu, Y. Jiang, H. Zhao, J. Chen, J. Cheng, K. Yang and Y. Li, *ACS Catal.*, 2016, **6**, 1097–1108.
23 X. Cheng, P. Dong, Z. Huang, Y. Zhang, Y. Chen, X. Nie and X. Zhang, *J. CO2 Util.*, 2017, **20**, 200–207.
24 D. Li, H. Haneda, N. K. Labhsetwar, S. Hishita and N. Ohashi, *Chem. Phys. Lett.*, 2005, **401**, 579–584.
25 J. Choi, H. Park and M. R. Hoffmann, *J. Phys. Chem. C*, 2010, **114**, 783–792.
26 J. C. Yu, J. G. Yu, W. K. Ho, Z. T. Jiang and L. Z. Zhang, *Chem. Mater.*, 2002, **14**, 3808–3816.
27 D. Wang, Z.-H. Zhou, H. Yang, K.-B. Shen, Y. Huang and S. Shen, *J. Mater. Chem.*, 2012, **22**, 16306–16311.
28 X. Yang, Y. Wang, L. Xu, X. Yu and Y. Guo, *J. Phys. Chem. C*, 2008, **112**, 11481–11489.
29 J. G. Yu, J. F. Xiong, B. Cheng and S. W. Liu, *Appl. Catal., B*, 2005, **60**, 211–221.
30 H. Tong, S. X. Ouyang, Y. P. Bi, N. Umezawa, M. Oshikiri and J. H. Ye, *Adv. Mater.*, 2012, **24**, 229–251.
31 H. L. Cui, W. Zhao, C. Y. Yang, H. Yin, T. Q. Lin, Y. F. Shan, Y. Xie, H. Gu and F. Q. Huang, *J. Mater. Chem.*, 2014, **2**, 8612–8616.
32 S. S. Kim, H. Lee, B. K. Na and H. K. Song, *Catal. Today*, 2004, **89**, 193–200.
33 X. D. Cheng, P. M. Dong, Z. F. Huang, Y. Z. Zhang, Y. Chen, X. X. Nie and X. W. Zhang, *J. CO2 Util.*, 2017, **20**, 200–207.
34 J. Qiu, S. Li, E. Gray, H. Liu, Q.-F. Gu, C. Sun, C. Lai, H. Zhao and S. Zhang, *J. Phys. Chem. C*, 2014, **118**, 8824–8830.
35 J. C. Parker and R. W. Siegel, *Appl. Phys. Lett.*, 1990, **57**, 943–945.
36 X. Lin, F. Rong, D. Fu and C. Yuan, *Powder Technol.*, 2012, **219**, 173–178.
37 C. Gunawan, W. Y. Teoh, C. P. Marquis, J. Lifia and R. Amal, *Small*, 2009, **5**, 341–344.
38 H. M. Sung-Suh, J. R. Choi, H. J. Hah, S. M. Koo and Y. C. Bae, *J. Photochem. Photobiol., A*, 2004, **163**, 37–44.
39 H. Zhao, F. Huang, J. Hou, Z. Liu, Q. Wu, H. Cao, Q. Jing, S. Peng and G. Cao, *ACS Appl. Mater. Interfaces*, 2016, **8**, 26675–26682.
40 M. Z. Ge, C. Y. Cao, S. H. Li, Y. X. Tang, L. N. Wang, N. Qi, J. Y. Huang, K. Q. Zhang, S. S. Al-Deyab and Y. K. Lai, *Nanoscale*, 2016, **8**, 5226–5234.
41 M. Pelaez, N. T. Nolan, S. C. Pillai, M. K. Seery, P. Falaras, A. G. Kontos, P. S. M. Dunlop, J. W. J. Hamilton, J. A. Byrne, K. O'Shea, M. H. Entezari and D. D. Dionysiou, *Appl. Catal., B*, 2012, **125**, 331–349.
42 S. N. Habisreutinger, L. Schmidt-Mende and J. K. Stolarczyk, *Angew. Chem., Int. Ed.*, 2013, **52**, 7372–7408.
43 E. Karamian and S. Sharifnia, *J. CO2 Util.*, 2016, **16**, 194–203.